Title
Early Tumor Detection by Active Feedback MR Molecular Imaging

Author
Dimitrov, Nikolay

Publication Date
2012

Peer reviewed|Thesis/dissertation

UNIVERSITY OF CALIFORNIA

Los Angeles

Early Tumor Detection by Active Feedback MR Molecular Imaging

A thesis submitted in the partial satisfaction

of the requirement for the degree Master of Science

in Chemistry

by

Nikolay Dimitrov Dimitrov

2012

ABSTRACT OF THE THESIS

Early Tumor Detection by

Active Feedback MR Molecular Imaging

by

Nikolay Dimitrov Dimitrov

Masters of Science in Chemistry

University of California, Los Angeles, 2012

Professor Yung-Ya Lin, Chair

Sensitive imaging of superparamagnetic nanoparticles or aggregates is of great importance in magnetic resonance molecular imaging and medical diagnosis. For this purpose, a conceptually new approach, termed "active feedback magnetic resonance", was developed. In the presence of the Zeeman field, a dipolar field is induced by the superparamagnetic nanoparticles or aggregates. Such dipolar field creates a spatial and temporal (due to water diffusion) variations to the precession frequency of the near-by water ^{1}H magnetization. Sensitive imaging of magnetic nanoparticles or aggregates can be achieved by manipulating the intrinsic spin dynamics by "selective self-excitation" and "fixed-point dynamics" under active feedback fields. Phantom experiments of superparamagnetic nanoparticles, *in vitro* experiments of brain tissue with blood clots, and *in vivo* mouse images of colon cancers labeled by magnetic nanoparticles suggest this new approach provide enhanced, robust, and positive contrast in imaging magnetic nanoparticles or aggregates for early lesion detection.

The thesis of Nikolay Dimitrov Dimitrov is approved.

_____

Albert Thomas

_____

William Gelbart

_____

Yung-Ya Lin, Committee Chair

University of California, Los Angeles

2012

TABLE OF CONTENTS

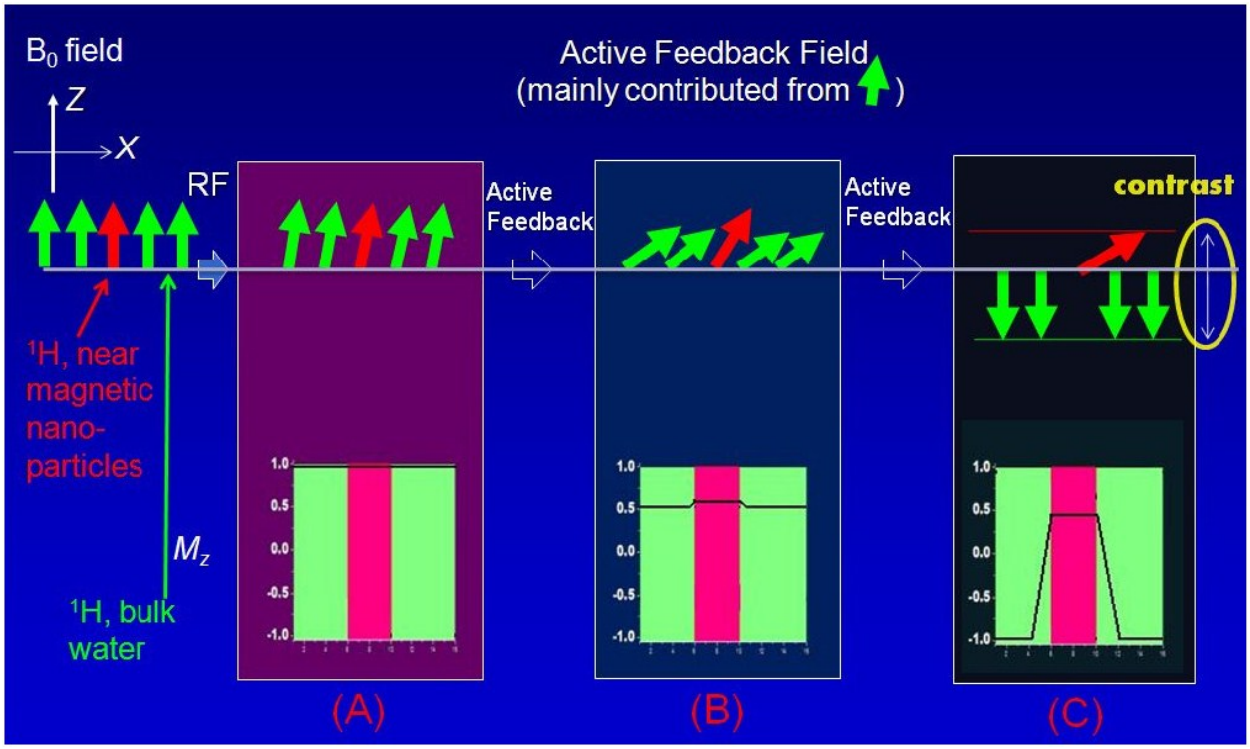

Figure 1. Contrast mechanism by "selective self-excitation" and "fixed-point dynamics" under active feedback fields. Red arrows denote the water ^{1}H magnetization near the center of the dipolar field, while the green arrows denote the bulk water ^{1}H magnetization far away from the dipole center. Under equilibrium condition, all magnetization lines up with external Zeeman field. (A) A small flip-angle (β=5-10º) RF pulse tilts the sample equilibrium magnetization. (B) Since the averaged transverse magnetization is mainly contributed from the bulk water ^{1}H spins, the resulting active feedback field generated by the active feedback electronic device possesses a frequency closer to that of the bulk water ^{1}H spins which are distant from the dipole center. By "selective self-excitation", the feedback field tilts the bulk water ^{1}H spins more effectively towards the stable fixed-point, –z-axis (assume feedback phase 180º), while the ^{1}H spins near the dipole center are less affected due to resonance mismatch. (C) This "selective self-excitation" process continues and enlarges the contrast between the longitudinal magnetization of the ^{1}H spins in bulk water and those near the dipole center. Maximum contrast in the longitudinal magnetization can be achieved and locked when the bulk water spin magnetizations evolve to the fixed point: all align along –z in this case.

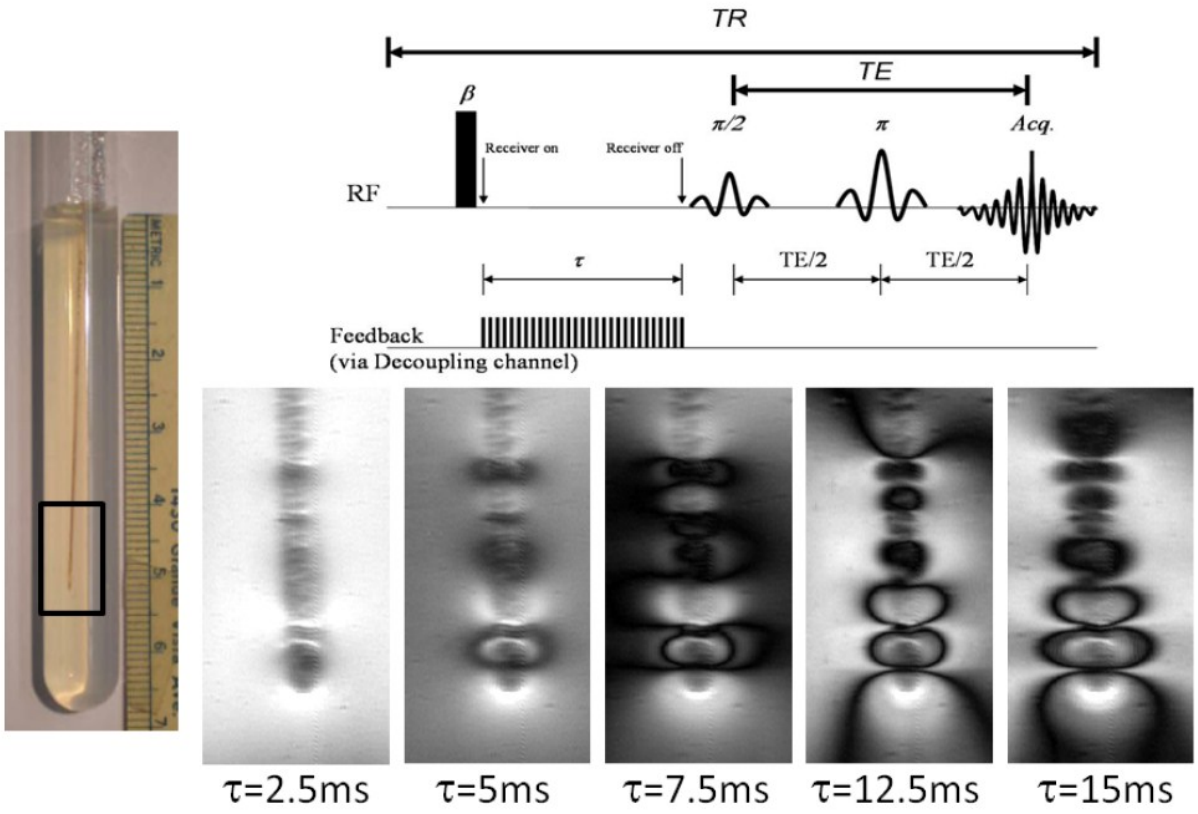

Figure 2. The active feedback pulse sequence for sensitive imaging of magnetic nanoparticles. Here shows the development of contrast in active feedback images, as demonstrated by a 10-mm cylindrical phantom sample consisting of agar with an inner capillary of 20-nm superparamagnetic nanoparticles with various degrees of aggregation. The parameters used in the pulse sequence are: initial RF pulse flip angle β=10º, feedback strength τ_{AF} = 1.2 ms, and feedback phase ψ =180º (ref. Eq. [2]). The evolution time under the active feedback field, τ, is noted under the corresponding images.

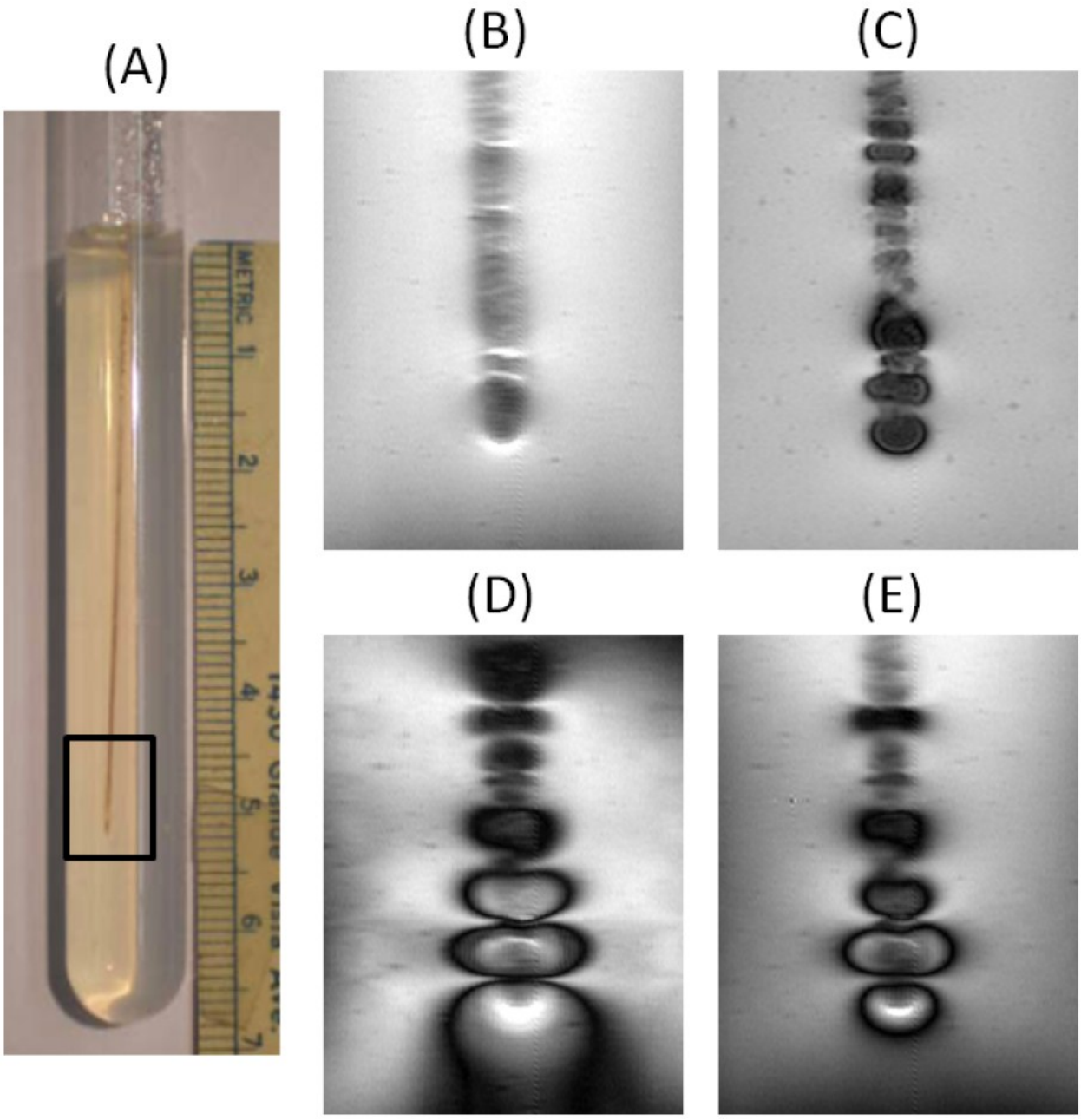

Figure 3. Sensitivity and contrast of the active feedback images to magnetic nanoparticles, compared with conventional T_2- and T_2*-weighted images, as demonstrated by a 10-mm cylindrical phantom sample consisting of agar with an inner capillary of 20-nm 16 superparamagnetic nanoparticles with various degrees of aggregation, shown in (A). (B) T2-weighted images acquired by spin-echo RARE pulse sequence. (C) T_2*-weighted images acquired by gradient-echo GEFI pulse sequence. (D) and (E) active feedback images acquired with feedback strength τAF =1.2 ms and 4.5 ms, respectively. The active feedback pulse sequence is shown in Fig. 2, followed by a spoiled gradient and spin-echo RARE acquisition (TE =4.2 ms and TR = 10 s).

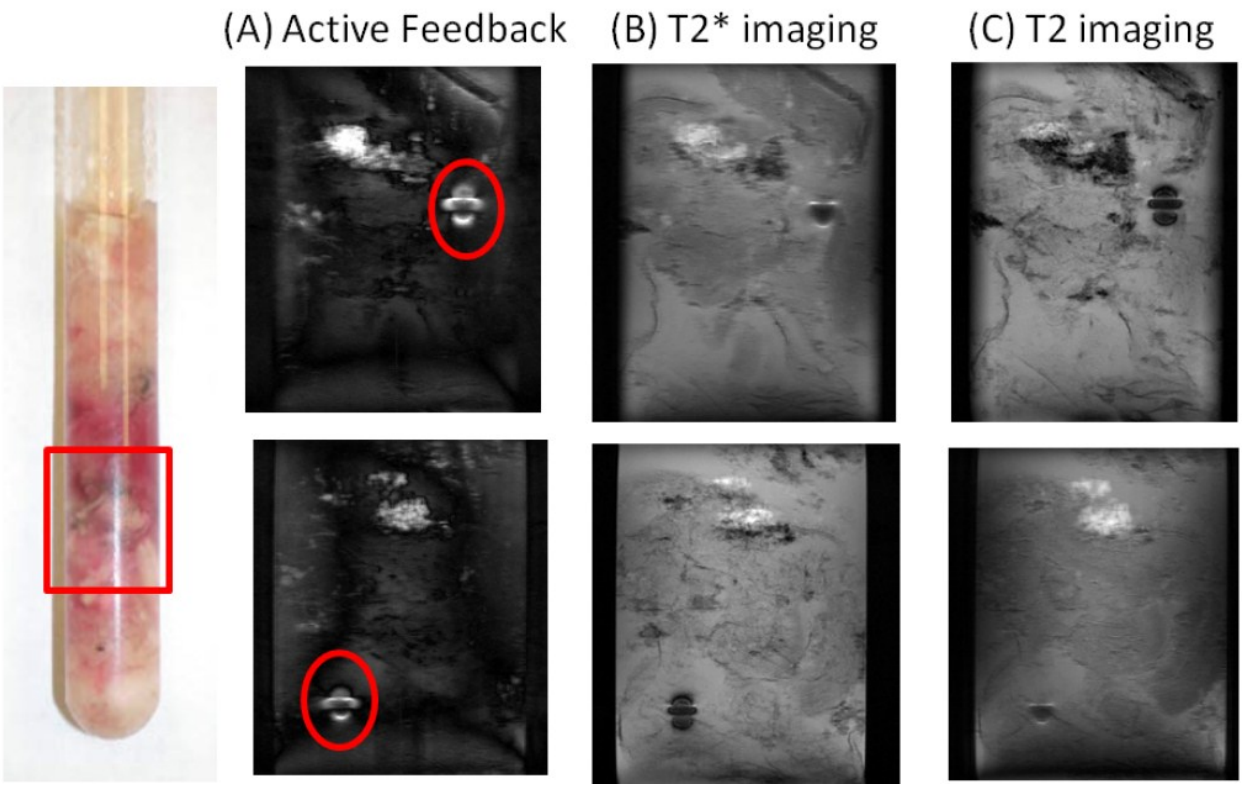

Figure 4. Demonstration of the potential applicability of the active feedback images for early stroke detection by lighting up the micro blood clot. Here show the active feedback images of *in vitro* brain tissue in a 10-mm tube excised from a patient undergoing intracranial surgery for glioblastoma multiforme, compared with conventional T_2- and T_2*-weighted images. (A) Active feedback images with feedback strength τ_{AF} =1.2 ms, evolution time τ = 10ms, and the pulse sequence is shown in Fig. 2, followed by a spoiled gradient and RARE acquisition with TE = 10.2 ms and TR = 10 s. (B) T_2*-weighted images acquired by gradient-echo GEFI pulse sequence. (C) T2-weighted images acquired by spin-echo RARE pulse sequence.

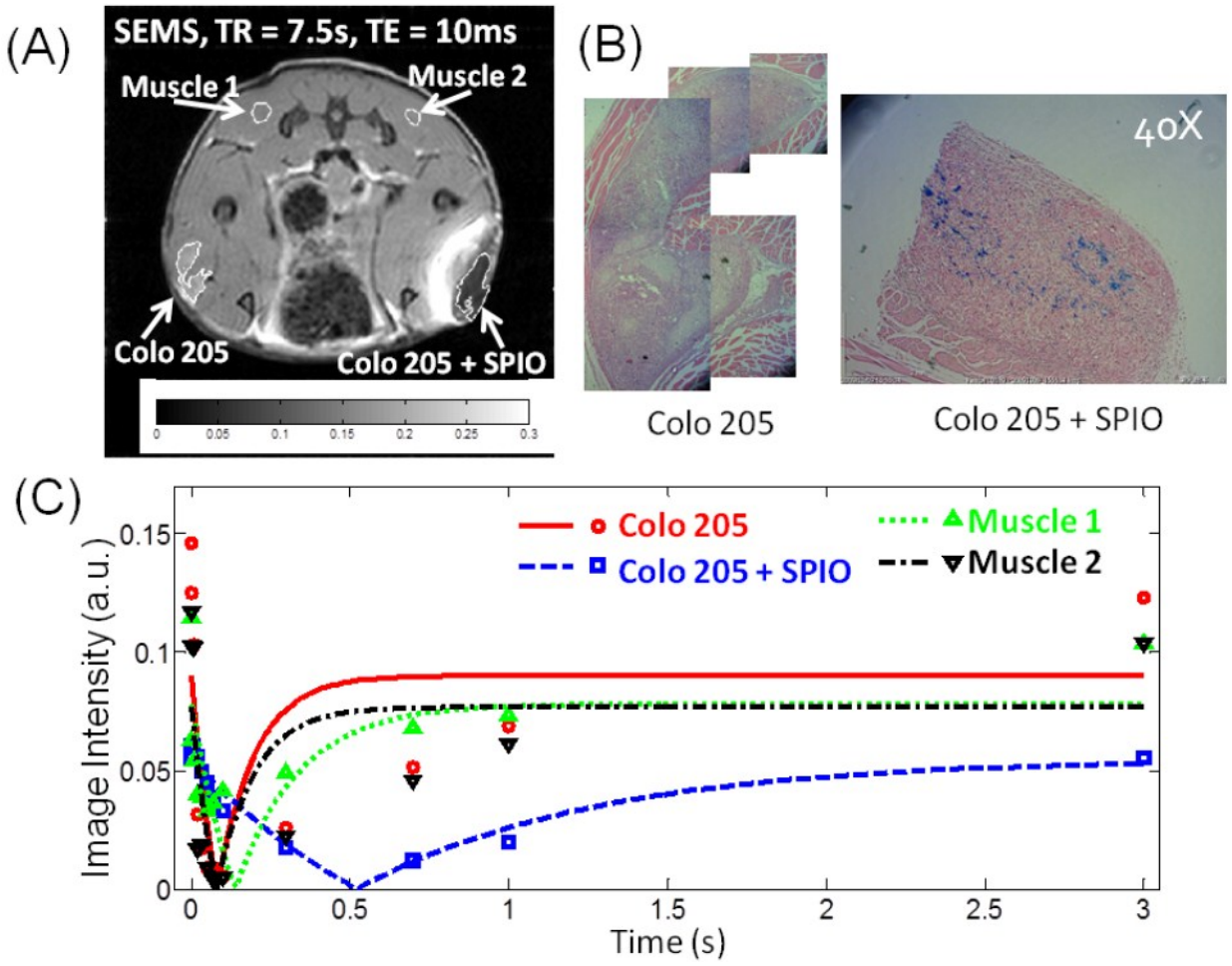

Figure 5. *In vivo* images of human colon cancers (COLO 205 human colon adenocarcinoma cell line) from nude mouse xenografts with magnetic nanoparticles (SPIO) labeled tumor cells at right flank and unlabeled tumor at left flan, FOV = 3 cm × 3 cm, and thickness = 1 mm. (A) Locations of the selected ROIs representing muscles, unlabeled tumor, and labeled tumor. (B) Histological section of both tumors at left and right flanks with Perls' Prussian blue to confirm the existence and distribution of SPIO. (C) Image intensity of active feedback imaging at various ROIs and active feedback evolution time (τ in the active feedback pulse sequence in Fig. 2), as fitted by T_1 inversion recovery formula to examine the extra contributions of "selective self-excitation" by active feedback fields in regions without SPIO to rotate the magnetization back to +z. Also see caption in Fig. 6.

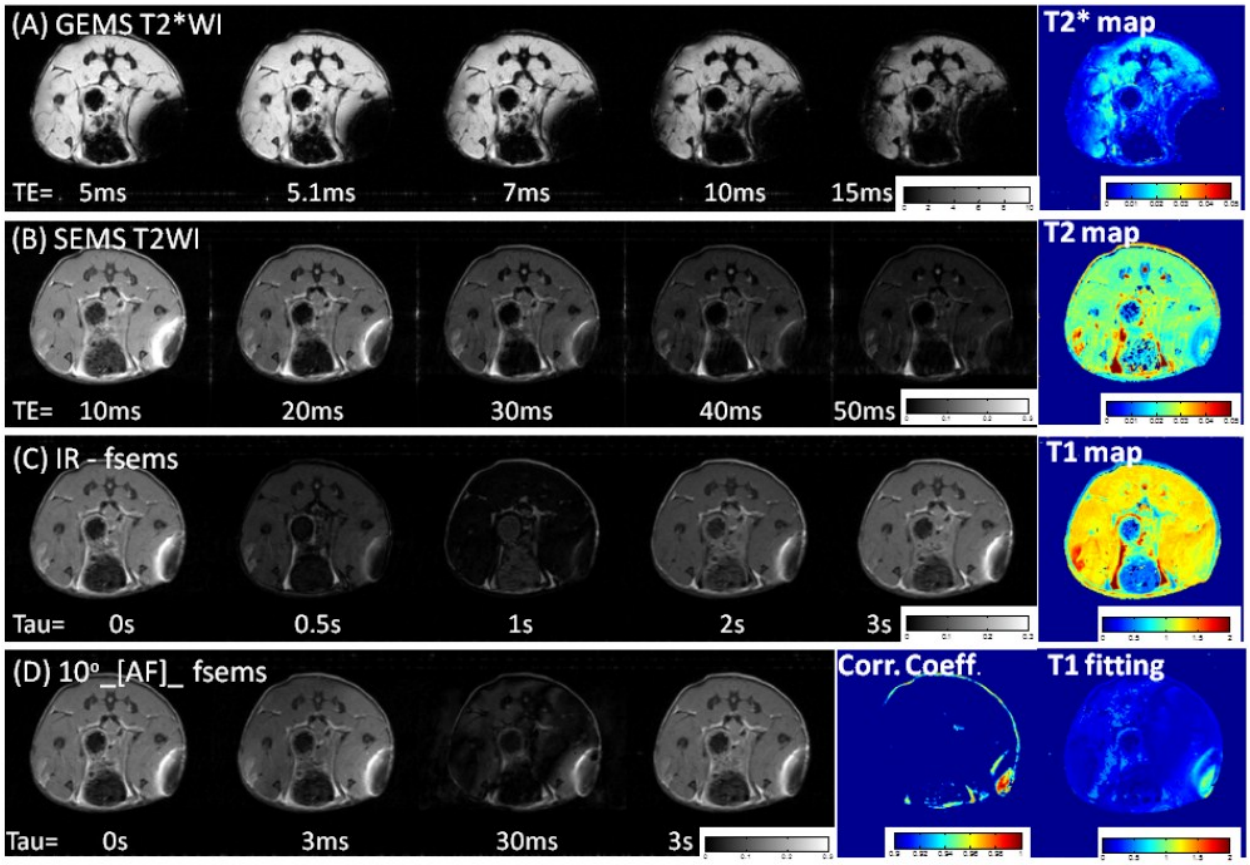

Figure 6. *In vivo* images and parameter mapping of human colon cancers (COLO 205 human colon adenocarcinoma cell line) from nude mouse xenografts with magnetic nanoparticles 17 (SPIO) labeled tumor cells at right flank and unlabeled tumor at left flan, FOV = 3 cm × 3 cm, and thickness = 1 mm. (A) T_2*-weighted image and T_2* parameter mapping. (B) T_2-weighted image and T_2* parameter mapping. (C) Inversion recovery T_1-weighted image and T1 parameter mapping. (D) active feedback image, T1 parameter mapping, and fitting-correlation-coefficient mapping (colorbar 0.9-1). As described in "Theory", due to resonance mismatch, the SPIO labeled tumor at right flank can resist "selective self-excitation" from the active feedback fields generated by the bulk water and the active feedback device. Therefore, the dynamics of its longitudinal magnetization is mainly T_1 relaxation with a longer T_1 time (as there is no "selective self-excitation" to help rotate the magnetization back to +z) and higher T_1 fitting-correlation-coefficient (as the dynamics is well described by T_1 inversion recovery). On the other hand, for muscles and unlabeled tumors, "selective self-excitation" rapidly rotates the bulk water magnetization back to the stable +z fixed-point with $\psi = 0^o$ (as if T_1 is short), creating spin dynamics very different from simple T_1 inversion recovery (lower T_1 fitting correlation coefficient).

AKNOWLEDGEMENT

I want to first thank my parents for their belief in my abilities and their support of my academic pursuits. I owe everything that I have achieved to them, because they believed in me, supported me and allowed to pursue my goals.

I thank Professor Yung-Ya Lin for his support, academic guidance, and inspiration to do research in science these past 3 years. He enriched my educational experience by giving me opportunities to go to conferences overseas, fostered my interest in the physical sciences and supported me completely in my academic endeavors.

My group mates, past and current, have been instrumental to the development of my research skills, including experimental techniques and coding in MATLAB. I thank them dearly for helping me excel as a researcher.

I would also like to thank the collaborators at the National Taiwan University for their contribution of the *in vivo* imaging experiments in this thesis: Chaohsiung Hsu, Hsin-Wei Chang, Dennis W. Hwang and Lian-Pin Hwang.

I would also like to acknowledge Zhao Li for drafting this manuscript and Professor Yung-Ya Lin for supervising the project as principal investigator.

This work was supported by the Camille and Henry Dreyfus Foundation (TC-05-053), NSF (CDI DMS 0833863 and CHE 1112574) and the Hirshberg Foundation for Pancreatic Cancer Research.

INTRODUCTION

Sensitive imaging of superparamagnetic nanoparticles (SPIO) and their aggregates is of great importance in magnetic resonance (MR) molecular imaging and medical diagnosis. Superparamagnetic nanoparticles serve as "molecular beacons" in molecular imaging and have found popular applications because of the following properties: their effects on contrast are stronger than those of paramagnetic nanoparticles, their magnetic properties can be manipulated by controlling their sizes and coating surfaces, and their iron-oxide basis gives them improved biocompatibility and biodegradability. Sensitive detection of superparamagnetic molecular aggregates may lead to improvements in medical diagnosis by MR imaging, because some pathological structures in the human body are analogous to such aggregates. For example, Alzheimer's Disease (AD) is characterized by aggregates (called plaques) of amyloid-beta protein that are high in ferritin, an iron storage protein found in the brain. Hemoglobin is the most important component of red blood cells, which is composed of heme and iron. Moreover, early-stage tumors are characterized by the formation of new blood vessels to supply tumors with oxygen and nutrients. Therefore, the challenges of early detection of Alzheimer's Disease, stroke, and tumor may be rendered into sensitive detection of the dipolar fields induced by magnetic nanoparticles or iron-containing molecular aggregates.

In the presence of the Zeeman field, a dipolar field is induced by the superparamagnetic nanoparticles or aggregates. Such dipolar field creates a spatial and temporal (due to water diffusion) variations to the precession frequency of the near-by water ^{1}H magnetization. The strong local magnetic-field gradient around the dipole center enhances the reversible inhomogeneous and irreversible homogeneous dephasing mechanisms to generate signal void and negative contrast in T_2- or T_2*-weighted images. Improved imaging specificity and

identification can be achieved through highlighting the dipole center with positive contrast. For this purpose, Cunningham et al. utilized spectrally selective radio-frequency (RF) pulses to excite and refocus the off-resonance water ^{1}H magnetization surrounding the dipole center to get a positive contrast (1). Zurikya and Hu presented a diffusion-mediated off-resonance saturation (ORS) method to generate contrast (2). Seppenwoolde et al. proposed the "white marker" technique and achieved positive contrast by dephasing the background signal with an unmatched gradient echo, while near the dipole center the signal is conserved because the induced dipolar field compensates the dephasing gradient (3). Mani et al. also achieved a positive contrast using gradient echo acquisition (4).

In this work, a conceptually new approach, termed "active feedback magnetic resonance", was developed to sensitively imaging superparamagnetic nanoparticles or aggregates with enhanced, robust, and positive contrast for early lesion detection. This approach is based on the feedback-induced nonlinear and chaotic spin dynamics that we discovered earlier (5). In summary, an active feedback electronic device was home-built and active feedback pulse sequences were devised to generate avalanching spin amplification, which enhances the weak dipolar-field perturbations from magnetic nanoparticles in phantom samples, blood clots, and tumors.

THEORY

Active Feedback Fields

Superparamagnetic nanoparticles or aggregates produce a local magnetic field inhomogeneity, resulting from the difference in magnetic susceptibility with respect to the background materials. The field distribution outside the nanoparticles or aggregates is described by a magnetic dipole, as given by:

$$B_{dip,z}(x,y,z) = c\frac{x^2+y^2-2z^2}{(x^2+y^2+z^2)^{5/2}}$$

$$c = \frac{B_0 \Delta\chi V}{4\pi} \qquad [1],$$

where Bo is the Zeeman field strength oriented along the +z-axis, and $\Delta\chi V$ describes the local magnetic dose of the dipole as the product of the difference of volume susceptibilities to the environment and the dipole volume (6). The induced dipolar field changes the precession frequency of the near-by water ^{1}H according to $\delta\omega=\gamma B_{dip,z}$ where γ is the gyromagnetic ratio of ^{1}H. The water ^{1}H experiences fluctuating magnetic fields due to diffusion within the dipolar field.

Sensitive imaging of magnetic nanoparticles or aggregates may be achieved by manipulating the intrinsic spin dynamics by "selective self-excitation" and "fixed-point dynamics" under active feedback fields. Following current MR hardware design, an active feedback field can be generated from the induced free induction decay (FID) current by electronic feedback circuits, as described by the equation:

$$B_{AF,+}(t) = \frac{1}{\tau_{AF}}\langle im_+(r,t)\rangle e^{-i\psi} \qquad [2],$$

where the active feedback field $B_{AF,+} \equiv B_{AF,x} + iB_{AF,y}$, magnetization $\boldsymbol{m(r,t)} = \boldsymbol{M(r,t)}/M_0$ is normalized with respect to the equilibrium magnetization density M_0 of pure water, and the

transverse magnetization $m_+ \equiv m_x + i m_y$ (7-9). The feedback phase ψ is related to the angle between the active feedback field vector $B_{AF,+}(t)$ and the averaged transverse magnetization vector $<m_{+(r,t)}>$. For example, ψ = 0° when feedback field vector $B_{AF,+}(t)$ lags behind the averaged transverse magnetization vector $<m_{+(r,t)}>$ by 90°. In this case, the active feedback field will drive the magnetization towards the stable fixed point along the +*z*-axis, just as the natural radiation damping effect, while an active feedback field corresponding to ψ =180° will drive the magnetization towards the stable fixed point along the –*z*-axis (7-9). The feedback time constant, τ_{AF}, characterizes the feedback strength; the shorter τ_{AF} is, the stronger the active feedback field. The radiation damping effect in high-field MR systems with high-Q probes is a passive feedback field with feedback phase ψ = 0°, driving magnetization towards the stable fixed point along the +*z*-axis.

Contrast Mechanism by "Selective Self-Excitation" and "Fixed-Point Dynamics"

The contrast mechanism by "selective self-excitation" and "fixed-point dynamics" under active feedback fields is illustrated in Fig. 1. First, a small-angle radio-frequency (RF) pulse (β=10° in Fig. 2) tilts the equilibrium magnetization (Fig. 1A). Since the averaged transverse magnetization vector $<m+(r,t)>$ is mainly contributed from the bulk water ^{1}H magnetization, the resulting active feedback field generated by the active feedback device (Eq. [2]) possesses a frequency much closer to the precession frequency of the bulk water ^{1}H that is far away from the dipole center. By "selective excitation", the feedback field self-excites the bulk water magnetization more effectively towards the –z-axis (assume feedback phase ψ= 180°), while the ^{1}H magnetization near the dipole center is less affected due to resonance mismatch (Fig. 1B). This "selective self-excitation" process continues and enlarges the contrast between the longitudinal water ^{1}H magnetization in bulk water and that near the dipole center (Fig. 1C). The images of the

longitudinal water ^{1}H magnetization, $m_z(r)$, can then be acquired by a strong z-gradient to spoil the transverse magnetization, a slice-selective excitation, and any existing imaging method. The contrast mechanism by "selective self-excitation" and "fixed-point dynamics" under active feedback fields is experimentally robust: the spin dynamics freezes and the contrast gets locked when the bulk water ^{1}H magnetization reaches the fixed point along the –z-axis (with ψ =180°) and therefore diminish the active feedback fields. In biomedical samples, the strong T_2/T_2* dephasing mechanisms can also crush the averaged transverse magnetization of the bulk water when it is self-excited to rotate to the xy plane from +z axis (with ψ =180°) and diminish the active feedback field, leaving the magnetization near SPIO along the +z direction to generate enhanced, positive contrast.

Similar contrast mechanism can be achieved in MR systems with strong radiation damping, which is a passive feedback field with feedback phase ψ = 0°. In this case, a large flip angle RF pulse (β =170°) tilts the equilibrium magnetization close to –z-axis, and then contrast develops on its way back to the +z-axis stable fixed-point by "selective self-excitation" from the passive feedback field of radiation damping (ψ = 0°).

MATERIALS AND METHODS

Active Feedback Device

The principle behind the active feedback electronic device is to filter, phase-shift, and amplify the signals from the receiver coils and then re-transmit the modified signal into the RF transmitter coils. Two major objectives in home-building the active feedback electronic device are: a (i) strong and (ii) controllable active feedback field. To fulfill this goal, digitally controlled phase shifter and amplifier were included in the feedback circuit so that the spectrometer hardware can control the trigger signal and the phase, gain, and duration of the active feedback fields. As a result, we are able to create active feedback pulse sequences that include regular RF fields and active feedback fields at a separate channel, allowing us to utilize the active feedback fields in novel ways. The tunable and programmable feedback phase and gain open new possibilities in pulse sequence design for innovative spin dynamics and applications.

Phantom and In Vitro Experiments

Phantom and in vitro experiments were performed on a 14.1-T spectrometer (Bruker Avance 600) equipped with a Micro5 gradient system with maximal gradient strength of 192 G/cm in three orthogonal directions. A 10-mm saddle coil optimized for proton sensitivity was used for RF transmission and reception. The active feedback time constant □AF was estimated by fitting the FIDs following a 10° RF pulse, taking into account the static field inhomogeneity. The 10-mm cylindrical phantom sample, shown in Figs. 2A and 3A, consists of agar with an inner capillary of superparamagnetic nanoparticles (OceanNanotech, 20nm diameter, coated with dextrin) with various degrees of aggregation. Care was taken to avoid the formation of air bubbles. The concentration of the superparamagnetic nanoparticles injected into the agar solution is 4.8 mg/mL.

For the *in vitro* brain tissue experiments shown in Fig. 4, samples were obtained from a patient undergoing intracranial surgery for glioblastoma multiforme (male, age 6). A 10-mmdiameter block was excised (not needed for immediate pathology examinations) and placed in a 10-mm MR sample tube filled with 0.9% sodium chloride solution.

The active feedback images were acquired using the sequence shown in Fig. 2, with β= 10°, feedback phase ψ=180°, a crusher z-gradient GT = 20 G·ms/cm, and RARE acquisition (TE = 4.2 ms, TR = 10 s). Conventional T_2*-weighted images by gradient-echo GEFI pulse sequence (Figs. 3C and 4B, TE = 20 ms, TR = 3 s) and conventional T_2-weighted images by spin-echo RARE pulse sequence (Figs. 3B and 4C, TE = 4.2 ms, TR = 10 s) were acquired for comparison. All images were acquired with the following parameters: sagittal 1-mm thick slices, 512×128 voxels zero-filled to 512×256 voxels, FOV 1.5 cm.

In Vivo Experiments

The COLO 205 cells, a human colon adenocarcinoma cell line expressing surface CA19-9 antibody, were purchased from American Type Culture Collection (Manassas, VA) and cultured in RPMI1640 medium (Gibco), supplemented with 10% heat-inactivated fetal bovine serum in a humidified atmosphere at 37°C with 5% CO_2.

To generate SPIO-labeled cells, COLO 205 cells were incubated for 24 h at 37°C in the serum-free RPMI medium which contains 75 μg SPIO (OceanNanotech, 20nm diameter, coated with dextrin) and 0.75 μg poly-Llysine (PLL, Sigma) per mL. After SPIO was engulfed by the cells, we washed out residual extracellular SPIO or PLL with fresh phosphate-buffered saline (PBS) three times.

Animal experiments were performed in accordance with the institutional guidelines. COLO 205 cells in 100ul PBS (106 cells) were injected subcutaneously into nude

BALB/cAnN.Cg-*Foxn1*nu/CrlNarl mice's (National Laboratory Animal Center, Taipei, Taiwan) left flank and SPIOlabeled COLO 205 cells were injected to the other side. During the scanning, mouse was manipulated under anesthesia (5% isoflurane induction, 2% for maintenance in air). The *in vivo* images were acquired on a Varian INOVA 7-T NMR microimaging spectrometer (Varian Inc., CA, USA) with an external home-built active feedback device. All images were acquired with matrix = 128×128, FOV (field of view) = 30x30 mm, slice thickness = 1mm. T2*WI images were acquired at Ernst condition with flip angle = 26°, TR = 150ms, number of scan = 16 and various TE = 5~15ms. For spin-echo T2WI images, TR = 7.5s, TE = 10~50ms. Inversion-recovery T1 and active feedback images were acquired with fast spin echo sequence with echo spacing = 10ms, number of echo = 4, and TR = 7.5s.

RESULTS

The spin dynamics described in "Theory" are first demonstrated and confirmed by a phantom sample consisting of superparamagnetic nanoparticle aggregates in agar solution. Images of the absolute value of the longitudinal water ^{1}H magnetization, $|m_z(r)|$, at various evolution times under the active feedback fields with feedback phase ψ=180° and feedback strength τ_{AF} = 1.2 ms are shown in Fig. 2. While the contrast develops continuously over time, the positive contrast of the water ^{1}H magnetization surrounding the dipole center is most obvious when the bulk water ^{1}H magnetization lies on the transverse plan (e.g., when evolution time τ= 7.5 ms). The void magnetization, $m_z(r) = 0$, around the dipole center shows that the longitudinal magnetization inside ($m_z(r) > 0$) and outside ($m_z(r) < 0$) the dark boundary possesses opposite signs. It is illustrated that active feedback imaging can sensitively and selectively highlight the different dipolar strength *c* (ref. Eq. [1]) corresponding to various sizes of superparamagnetic nanoparticle aggregates.

Sensitivity and contrast of the active feedback imaging to magnetic nanoparticles, compared with conventional T_2- and T_2*-weighted imaging, are shown in Fig. 3, using the same sample as in Fig. 2. The spatial extent of the imaged dipolar field reflects the relative sensitivity in imaging magnetic nanoparticles.

Figure 4 shows the *in vitro* active feedback images of brain tissue removed from the left posterior parietal occipital lobe of a 6-year-old boy with glioblastoma multiforme. The active feedback image shows intense positive contrast in regions with greater concentrations of deoxyhemoglobin from blood clots, consistent with the darker regions in the T_2*-weighted and T_2-weighted images corresponding to increased dephasing.

Mouse models infected with human colon cancer cell line COLO 205 were imaged. Representative results are shown in Figs. 5 and 6. As a control, the tumor at right flank is labeled with magnetic nanoparticles, while the other is not. ROIs that represent muscles, unlabeled tumor, and labeled tumor are first defined (Fig. 5A). The existence and distribution of magnetic nanoparticles is confirmed by Perls' Prussian blue iron-stain histology. Active feedback image intensity, acquired with initial RF flip angle β=170° and feedback phase ψ=0°, for various active feedback evolution time τ is fitted by T_1 inversion recovery formula to detect the existence and significance of "selective self-excitation" at the locations of muscles, SPIO-labeled tumor, and unlabeled tumor. As described in "Theory", due to resonance mismatch, the SPIO labeled tumor at right flank can resist "selective self-excitation" from the active feedback fields generated by the bulk water and the active feedback device. Therefore, the dynamics of its longitudinal magnetization is mainly T_1 relaxation with a longer T_1 time (as there is no "selective self-excitation" to help rotate the magnetization back to +z) and higher T_1 fitting-correlation-coefficient (as the dynamics is well described by T_1 inversion recovery). On the other hand, for muscles and unlabeled tumors, "selective self-excitation" rapidly rotates the bulk water magnetization back to the stable +z fixed-point with ψ=0° (as if T_1 is short), creating spin dynamics very different from simple T_1 inversion recovery (lower T_1 fitting correlation coefficient).

While conventional T_2* parameter mapping (Fig. 6A) and T_2 parameter mapping (Fig. 6B) can hint at the location of the SPIO-labeled tumor, the T_1 parameter mapping and fitting-correlation-coefficient mapping (Fig. 6D) from active feedback images clearly highlight the tumor mass with a close correlation of the size with iron-stain histopathology.

DISCUSSION & CONCLUSION

The observed contrast by "selective self-excitation" and "fixed-point dynamics" under active feedback fields can also be understood by considering the dependence of this contrast mechanism on the frequency offsets of different water ^{1}H frequency components (also called "spectral packets") as well as the relative contribution of each frequency component to the total magnetization, as applied to a dipolar field distribution. Such dipolar fields taper off quickly as a function of $1/r^3$ and span several voxels. Consequently, magnetization in the immediate vicinity of the dipole experiences a larger frequency shift and wider distribution of resonance frequencies, compared with the smaller shift and narrower distribution of frequencies for magnetization farther from the center of the dipole. Following a 10° RF pulse, the magnetization farther away from the dipole center is nutated by the active feedback field (with feedback phase ψ=180°) toward $-z$–axis more quickly, crossing the transverse plane earlier. On the other hand, the magnetization closer to the dipole center experiences significantly different field strength and is much less excited by the dynamics under active feedback fields. The resulting absolute-value longitudinal-magnetization image, $|m_z(r)|$, thus displays the magnetization surrounding the dipole as regions of bright contrast with darkened boundary, as shown in Figs. 2 and 3.

Active feedback fields with tunable, programmable feedback strength and phase could provide added flexibility by altering the functional dependence of the feedback fields on the averaged transverse magnetization (Eq. [2]). As such, active feedback fields introduce a conceptually new approach to practicing magnetic resonance by adding a new line to the pulse sequences and by allowing for additional control over the spin dynamics. Active feedback differs fundamentally from externally applied RF pulses in that the interplay between the magnetization and the feedback fields allows the spins to direct their own evolution.

For example, “selective self-excitation” and “fixed-point dynamics” under active feedback fields show promises in generating enhanced, robust, and positive contrast, reflecting microscopic field variations such as those induced by local dipolar fields, e.g., in cells labeled with superparamagnetic nanoparticles. This is in distinction to the negative contrast seen in T_2-weighted or T_2*-weighted images, which can hinder the direct evaluation of surrounding tissues and discrimination between target molecules/cells and susceptibility artifacts. As active feedback fields can be viewed as selective RF fields generated by the magnetization itself, mediated through coupling with the receiver coil and then controlled by the electronic feedback circuits, the feedback fields may be used to highlight off-resonance water ^{1}H magnetization surrounding a dipole to yield more detailed, bright contrast, as demonstrated experimentally on aggregates of superparamagnetic nanoparticles (Figs. 2 and 3), on blood clots in freshly excised brain tissue (Fig. 4), and on SPIO-labeled colon cancers (Figs. 5 and 6).

In conclusion, the spin dynamics originated from “selective self-excitation” and “fixedpoint dynamics” under active feedback fields have been shown to be sensitive to dipolar fields generated by magnetic nanoparticles. Phantom, *in vitro*, and *in vivo* experimental results indicate that this approach generates enhanced, robust, and positive contrast, reflecting microscopic field variations induced by strong local dipole fields, such as those created by superparamagnetic nanoparticles or iron-containing molecular aggregates. Statistical results (N>10) for mouse models at various cancer stages and alternative active feedback pulse sequences with further improved performance shall be reported at a later occasion.

REFERENCES

(1) Cunningham CH, Arai T, Yang PC. Positive Contrast Magnetic Resonance Imaging of Cells Labeled with Magnetic Nanoparticles. Magn Reson Med 2005; 53: 999-1005.

(2) Zurkiya O, Hu X. Off-resonance Saturation as a Means of Generating Contrast with Superparamagnetic Nanoparticles. Magn Reson Med 2006; 56: 726-32.

(3) Seppenwoolde JH, Viergever MA, Bakker CJ. Passive Tracking Exploiting Local Signal Conservation: the White Marker Phenomenon. Magn Reson Med 2003; 50: 784-90.

(4) Mani V, Briley-Saebo KC, Itskovich VV. Gradient Echo Acquisition for Superparamagnetic Particles with Positive Contrast (GRASP): Sequence Characterization in Membrane and Glass Superparamagnetic Iron Oxide Phantoms at 1.5 T and 3 T. Magn Reson Med 2006; 55: 126-135.

(5) Lin YY, Lisitza N, Ahn S, Warren WS. Resurrection of crushed magnetization and chaotic dynamics in solution NMR spectroscopy. Science 2000; 290: 118-21.

(6) Broekaer P, Jeener J. Suppression of Radiation Damping in NMR in Liquids by Active Electronic Feedback. J Magn Reson A 1995; 113: 60-64.

(7) Abergel D, Louis-Joseph A, Lallemand JY. Amplification of Radiation Damping in a 600-MHz NMR Spectrometer: Application to the Study of Water-Protein Interactions. J Biomol NMR 1996; 8: 15-22.

(8) Huang SY, Anklin C, Walls JD, Lin YY. Sizable Concentration-Dependent Frequency Shifts in Solution NMR Using Sensitive Probes. J Am Chem Soc 2004; 126: 15936-15937.

(9) Huang SY, Yang SS, Lin YY. Sensitivity of Feedback-Enhanced MRI Contrast to Macroscopic and Microscopic Field Variations. Magn Reson Med 2009; 61: 925-36.